


 Cite this: *RSC Adv.*, 2022, **12**, 9883

## Optoelectronic properties and interfacial interactions of two-dimensional $\text{Cs}_2\text{PbX}_4\text{--MSe}_2$ ( $\text{M} = \text{Mo, W}$ ) heterostructures

 Ying Jie Chen,<sup>ab</sup> Xue Li,<sup>b</sup> Bao Nan Jia,<sup>b</sup> Chao Dong,<sup>b</sup> Xiao Ning Guan,<sup>b</sup>  Xin Zhao<sup>a</sup> and Li Hong Han<sup>\*abc</sup>

Constructing 2D inorganic perovskites and TMDs heterostructures is an effective method to design stable and high-performance perovskites optoelectronic applications. Here, we investigate the optoelectronic properties and interfacial interactions of  $\text{Cs}_2\text{PbX}_4\text{--MSe}_2$  ( $\text{X} = \text{Cl, Br, I}; \text{M} = \text{Mo, W}$ ) heterostructures using first-principles calculations. Firstly, six  $\text{Cs}_2\text{PbX}_4\text{--MSe}_2$  interfaces remain stable in energy. With the halogen varying from Cl to I, the interlayer distances of  $\text{Cs}_2\text{PbX}_4\text{--MSe}_2$  heterostructures increase rapidly. The CBM and VBM of monolayer  $\text{Cs}_2\text{PbX}_4$  are all higher than that of monolayer  $\text{MSe}_2$  and the charges transfer from  $\text{Cs}_2\text{PbX}_4$  interfaces to  $\text{MSe}_2$  interfaces when they contact. Both  $\text{Cs}_2\text{PbX}_4\text{--MSe}_2$  heterostructures are type-II heterostructures, which can drive the photogenerated electrons and holes to move in opposite directions. What's more,  $\text{Cs}_2\text{PbCl}_4\text{--MoSe}_2$  heterostructures exhibit the highest charge transport efficiency among  $\text{Cs}_2\text{PbX}_4\text{--MSe}_2$  heterostructures because  $\text{Cs}_2\text{PbCl}_4\text{--MoSe}_2$  heterostructures have the lowest exciton binding energies among  $\text{Cs}_2\text{PbX}_4\text{--MSe}_2$  heterostructures. In addition, the optical absorptions of all heterostructures are significantly higher than the corresponding  $\text{Cs}_2\text{PbX}_4$  monolayers and  $\text{MSe}_2$  monolayers. The construction of  $\text{Cs}_2\text{PbX}_4\text{--MoSe}_2$  heterostructures is beneficial for improving the photoelectric performance of two-dimensional perovskite devices. Lastly, we found that the  $\text{Cs}_2\text{PbI}_4\text{--WSe}_2$  heterostructure has the largest PCE (18%) among  $\text{Cs}_2\text{PbX}_4\text{--MSe}_2$  heterostructures. The  $\text{Cs}_2\text{PbCl}_4\text{--MoSe}_2$  heterostructure exhibits great potential application in photodetector devices and the  $\text{Cs}_2\text{PbI}_4\text{--WSe}_2$  heterostructure has great potential application in solar cells.

 Received 28th January 2022  
 Accepted 6th March 2022

DOI: 10.1039/d2ra00595f

[rsc.li/rsc-advances](http://rsc.li/rsc-advances)

## Introduction

Solar energy is a renewable and clean energy source that can be used in the field of solar cells. In the early years, perovskites were considered to be one of the most promising solar cell materials.<sup>1</sup> Three-dimensional (3D) lead halide perovskites have been innovatively applied in the field of solar cells with power conversion efficiency (PCE) up to 25.6%.<sup>2</sup> The high PCE of 3D lead halide perovskites is because of their excellent photoelectric properties, such as high carrier mobility, large light absorption coefficient, long carrier diffusion length and strong photoluminescence.<sup>3,4</sup> Although the three-dimensional lead halide perovskites have great photoelectric properties, their instability in air limits their widespread use for

commercialization.<sup>5,6</sup> In recent years, two-dimensional (2D) inorganic halide perovskites with good moisture resistance and stability have attracted attention for optoelectronic applications.<sup>7</sup> Currently, many theoretical studies and experiments on 2D perovskites have been conducted. For example, Ding *et al.* reported that the number of layers would affect the optical absorption and transport properties of 2D perovskite  $\text{Cs}_2\text{PbI}_4$ .<sup>8</sup> In addition, Bala *et al.* also revealed the same laws that the band gap and optical properties of 2D  $\text{Cs}_{n+1}\text{Pb}_n\text{X}_{3n+1}$  ( $\text{X} = \text{Cl, Br, I}$ ) perovskite vary with layer number.<sup>9</sup> In experiments, Song *et al.* fabricated 2D  $\text{CsPbBr}_3$  nanosheets and used them to produce high-performance photodetectors.<sup>10</sup> These studies found that the bandgaps of 2D monolayer lead halide perovskites are larger than 3D lead halide perovskites, which lead to lower electric properties, optical absorption and low performance of optoelectronic applications.

Fortunately, two-dimensional monolayer lead halide perovskites have a wide range of photoelectric properties adjustable by replacing halogens, changing layers, and working with other two-dimensional materials. In particular, the halide perovskites grown in the other 2D materials provides excellent ability to further adjust band gaps, transport properties, charge carrier dynamics, chemical stability and optical light absorption.<sup>11</sup>

<sup>a</sup>State Key Laboratory of High Power Semiconductor Lasers, Changchun University of Science and Technology, Changchun 130013, China

<sup>b</sup>State Key Laboratory of Information Photonics and Optical Communications, Beijing University of Posts and Telecommunications, Beijing 100876, China

<sup>c</sup>School of Electronic Engineering, Beijing University of Posts and Telecommunications, Beijing 100876, China. E-mail: hanlhstar@bupt.edu.cn

<sup>d</sup>School of Information and Communication Engineering, Beijing University of Posts and Telecommunications, Beijing 100876, China. E-mail: guanxiaoning@bupt.edu.cn



Therefore, a great deal of scientific researches of 2D halide perovskites and 2D materials interface engineering have been carried to achieve low-cost, high efficiency, stable heterostructures photoelectric devices. For instance, He *et al.* theoretically studied the effects of different terminals of heterojunctions and found that  $\text{CsPbI}_3/\text{MoS}_2$  heterostructure had higher electric performances than  $\text{CsPbI}_3/\text{WS}_2$ .<sup>12</sup> The  $\text{WS}_2\text{--CsPbBr}_3$  heterostructure was applied to perovskite solar cells (PSCs), which significantly improved PSCs stability under constant light and humidity (80%) attack over.<sup>13</sup> While, the PCE of  $\text{WS}_2\text{--CsPbBr}_3$  PSCs is only 10.65%.<sup>13</sup> Recently, inverted perovskite solar cells with  $\text{WS}_2$  interlayers had increased PCE up to 21.1%.<sup>14</sup> As we can see, 2D lead halide perovskites applying for PSCs have high stability and can effectively improve PCE by coordinating with two-dimensional transition metal dichalcogenides (TMDs) such as  $\text{WS}_2$ ,  $\text{MoS}_2$  and so on.

$\text{MoSe}_2$  and  $\text{WSe}_2$  as conventional materials of TMDs are widely used in interface engineering in experiments to improve optoelectronic properties of 2D organic halide perovskites. In experiments, Lu *et al.* fabricated a high-Performance  $\text{WSe}_2\text{--CH}_3\text{NH}_3\text{PbI}_3$  perovskite photodetector.<sup>15</sup>  $\text{MoSe}_2\text{--CsPbBr}_3$  Mixed van der Waals nanohybrids shown higher photocurrent than pure  $\text{CsPbBr}_3$  nanocrystals.<sup>16</sup> Lee *et al.* found photoluminescence (PL) quenching occurred after the hybridization of perovskites with  $\text{MoSe}_2$  and  $\text{WSe}_2$  layers, which reflects the charge-transfer effect.<sup>17</sup> The PCE of PEDOT:PSS perovskite solar cells with  $\text{WSe}_2$ -mediated and without  $\text{WSe}_2$ -mediated is 16.3% and 13.8%, respectively.<sup>18</sup> These experiments observed the construction of TMDs and perovskite heterostructures can effectively improve the optoelectronic properties of halide perovskites. However, interface electronic transfer and band alignment of  $\text{Cs}_2\text{PbX}_4\text{--MSe}_2$  heterostructures are not studied theoretically. It's worth revealing the effect of halide elements and  $\text{MSe}_2$  ( $\text{M} = \text{Mo, W}$ ) on  $\text{Cs}_2\text{PbX}_4\text{--MSe}_2$  heterostructures, which can promote the development of 2D inorganic halide perovskite and TMDs optoelectronic applications.

Herein, we constructed the 2D inorganic halide perovskite  $\text{Cs}_2\text{PbX}_4$  ( $\text{X} = \text{Cl, Br, I}$ ) and monolayer  $\text{MSe}_2$  heterostructures and discussed their stability, photoelectric properties and charge transfer mechanism through first-principles calculations. We studied electronic structures of the heterostructures with different halide elements and analysed the band alignment type for comparison. Next, we explore the charge transfers mechanism by calculating charge density difference. Finally, optical absorption coefficients of monolayer  $\text{MSe}_2$ ,  $\text{Cs}_2\text{PbX}_4$  and heterostructures  $\text{Cs}_2\text{PbX}_4\text{--MSe}_2$  were calculated. Our results will be helpful to improve the application performance of two-dimensional lead halide perovskite and TMDs heterostructures.

## Computational details

All the density functional theory calculations were performed with the Vienna Ab initio Simulation Package (VASP) code.<sup>19,20</sup> The projector-augmented wave (PAW) method was referred to electron-ion interactions.<sup>21</sup> The structure-relaxation, interface binding energy and optoelectronic properties were computed by Perdew, Burke and Ernzerhof's (PBE) exchange correlation

function within the generalized gradient approximation (GGA) formalism.<sup>22–26</sup> The band gaps of monolayer perovskites and TMDs were further corrected using the screened Heyd–Scuseria–Ernzerhof (HSE) hybrid density functional with the spin-orbital coupling (SOC). The plane wave basis set with a cutoff energy of 450 eV. The convergence criteria were  $1 \times 10^{-4}$  eV for the self-consistent field energy and 0.01 eV  $\text{\AA}^{-1}$  for the residual forces on each atom, respectively. A vacuum of 20  $\text{\AA}$  was considered along  $z$  direction to avoid artificial interlayer interactions.  $3 \times 6 \times 1$   $k$ -sampling generated by the Monkhorst–Pack scheme for the Brillouin zone was adopted. The zero damping DFT-D3 method of Gimme is used to account for correcting the van der Waals interaction of Heterostructure.

The interface binding energy is calculated by the following formula:

$$E_b = (E_{\text{heter.}} - E_{\text{Cs}_2\text{PbX}_4} - E_{\text{MSe}_2})/A \quad (1)$$

where  $A$  represents the interfacial area of  $\text{Cs}_2\text{PbX}_4\text{--MSe}_2$  heterostructures,  $E_{\text{heter.}}$ ,  $E_{\text{Cs}_2\text{PbX}_4}$ ,  $E_{\text{MSe}_2}$  are the total energy of heterostructures  $\text{Cs}_2\text{PbX}_4\text{--MSe}_2$ , monolayer  $\text{Cs}_2\text{PbX}_4$  and  $\text{MSe}_2$ , respectively.

The plane-averaged charge density difference  $\Delta\rho$  is calculated as the followed equation:

$$\Delta\rho(z) = \rho_{\text{heter.}} - \rho_{\text{Cs}_2\text{PbX}_4} - \rho_{\text{MSe}_2} \quad (2)$$

where  $\rho_{\text{heter.}}$ ,  $\rho_{\text{Cs}_2\text{PbX}_4}$  and  $\rho_{\text{MSe}_2}$  correspond to the plane-averaged charge density of heterojunctions  $\text{Cs}_2\text{PbX}_4\text{--MSe}_2$ , monolayer  $\text{Cs}_2\text{PbX}_4$  and  $\text{MSe}_2$ , respectively.

The 2D Mott–Wanani (MW) exciton binding energy ( $E_{\text{eb}}$ ) equation is calculated as the followed equation:

$$E_{\text{eb}} = 4 \frac{13.6\mu_{\text{ex}}}{m_0\epsilon^2} \text{ eV} \quad (3)$$

where  $\mu_{\text{ex}}$  is the effective exciton mass ( $\mu_{\text{ex}} = m_e m_h / (m_e + m_h)$ ),  $m_0$  is the electron mass, and  $\epsilon$  is the static dielectric constant. The effective masses of electron ( $m_e$ ) and hole ( $m_h$ ) are determined by the curvature of the energy band extremum.

The optical absorption coefficients are obtained from dielectric function, as the followed equation represented:

$$\alpha(\omega) = (\sqrt{2})\omega \left[ \sqrt{\varepsilon_1(\omega)^2 + \varepsilon_2(\omega)^2} - \varepsilon_1(\omega) \right]^{1/2} \quad (4)$$

$$\varepsilon(\omega) = \varepsilon_1(\omega) + i\varepsilon_2(\omega) \quad (5)$$

where  $\alpha$ ,  $\omega$  correspond to the optical absorption coefficient, the angular frequency and the dielectric function  $\varepsilon(\omega)$  contains real part  $\varepsilon_1(\omega)$  and imaginary part  $\varepsilon_2(\omega)$ .

## Results and discussion

In recent years, the 2D inorganic perovskites  $\text{Cs}_2\text{PbX}_4$  ( $\text{X} = \text{Cl, Br, I}$ ) and monolayers  $\text{MSe}_2$  ( $\text{M} = \text{Mo, W}$ ) have been successfully synthesized, which attracted much attention due to its highly stable structures.<sup>7,27,28</sup> The unit cell of  $\text{Cs}_2\text{PbX}_4$  perovskites belongs to cubic system and the optimized lattice parameters of



monolayer  $\text{Cs}_2\text{PbCl}_4$ ,  $\text{Cs}_2\text{PbBr}_4$ ,  $\text{Cs}_2\text{PbI}_4$  is 5.64 Å, 5.91 Å and 6.30 Å, respectively.<sup>29</sup>  $[\text{CsI}]^0$  interface exhibits more strongly charge transferring than  $[\text{PbI}_2]^0$ .<sup>30</sup> Therefore the  $[\text{CsI}]^0$  plane of the monolayer  $\text{Cs}_2\text{PbX}_4$  is used to form the heterojunctions. The optimized lattice parameters of monolayer  $\text{MoSe}_2$ ,  $\text{WSe}_2$  are 3.32 Å.<sup>31-33</sup> To minimize the lattice mismatch between the stacking blocks, the supercell of new  $\text{Cs}_2\text{PbX}_4\text{-MSe}_2$  heterostructures are built by  $3 \times 1$  cubic phases  $\text{Cs}_2\text{PbCl}_4$  and  $5 \times \sqrt{3}$   $\text{MSe}_2$ ,  $\sqrt{8} \times 2$  cubic phases  $\text{Cs}_2\text{PbBr}_4$  and  $5 \times \sqrt{13}$   $\text{MSe}_2$ , and  $\sqrt{8} \times \sqrt{2}$  cubic phases  $\text{Cs}_2\text{PbI}_4$  and  $\sqrt{31} \times \sqrt{7}$   $\text{MSe}_2$ , respectively, as seen in Fig. 1 (Table 1).

The lattice mismatches of  $\text{Cs}_2\text{PbCl}_4\text{-MoSe}_2$ ,  $\text{Cs}_2\text{PbBr}_4\text{-MoSe}_2$ ,  $\text{Cs}_2\text{PbI}_4\text{-MoSe}_2$ ,  $\text{Cs}_2\text{PbCl}_4\text{-WSe}_2$ ,  $\text{Cs}_2\text{PbBr}_4\text{-WSe}_2$  and  $\text{Cs}_2\text{PbI}_4\text{-WSe}_2$  heterostructures are less than 1.10%, 0.62%, 1.79%, 1.02%, 0.65% and 1.82%. The optimized vertical interlayer distances of  $\text{Cs}_2\text{PbCl}_4\text{-MoSe}_2$ ,  $\text{Cs}_2\text{PbBr}_4\text{-MoSe}_2$ ,  $\text{Cs}_2\text{PbI}_4\text{-MoSe}_2$ ,  $\text{Cs}_2\text{PbCl}_4\text{-WSe}_2$ ,  $\text{Cs}_2\text{PbBr}_4\text{-WSe}_2$  and  $\text{Cs}_2\text{PbI}_4\text{-WSe}_2$  interfaces are 3.07, 3.12, 3.16, 2.90, 3.18 and 3.30 Å, respectively, which increase gradually with the halogen varying from Cl to I. Interface binding energy of  $\text{Cs}_2\text{PbCl}_4\text{-MoSe}_2$ ,  $\text{Cs}_2\text{PbBr}_4\text{-MoSe}_2$  and  $\text{Cs}_2\text{PbI}_4\text{-MoSe}_2$ ,  $\text{Cs}_2\text{PbCl}_4\text{-WSe}_2$ ,  $\text{Cs}_2\text{PbBr}_4\text{-WSe}_2$  and  $\text{Cs}_2\text{PbI}_4\text{-WSe}_2$  interfaces is  $-16.73$ ,  $-16.28$  and  $-16.12$ ,  $-17.09$ ,  $-17.52$  and  $-15.56$  meV Å<sup>-2</sup>, respectively. The small interface binding energy and the interlayer distance ranging from 2.9 Å to 3.3 Å indicate that 2D  $\text{Cs}_2\text{PbX}_4\text{-MSe}_2$  heterostructures are formed by vdW contact.<sup>33</sup> These  $E_b$  values are comparable to  $E_b$  of  $\text{InSe}/\text{GaSe}$  ( $-18.25$  meV Å<sup>-2</sup>), suggesting that  $\text{Cs}_2\text{PbX}_4\text{-MSe}_2$  heterostructures are stable in energy.<sup>34</sup> In addition,  $\text{MoSe}_2\text{-CsPbBr}_3$  Mixed van der Waals nanohybrids also have been fabricated in experiments (Table 2).<sup>16</sup>

In order to study the band structures of  $\text{Cs}_2\text{PbX}_4\text{-MSe}_2$  heterostructures, the band structures of 2D perovskites  $\text{Cs}_2\text{PbX}_4$ , monolayer  $\text{WSe}_2$  and monolayer  $\text{MoSe}_2$  were calculated by different functionals, including PBE, PBE with SOC (PBE + SOC), HSE, and HSE with SOC (HSE + SOC) functionals. Monolayer  $\text{MoSe}_2$  and monolayer  $\text{WSe}_2$  show a direct band gap of 1.45 eV and 1.56 eV using PBE functional. Monolayer

$\text{Cs}_2\text{PbCl}_4$ ,  $\text{Cs}_2\text{PbBr}_4$  and  $\text{Cs}_2\text{PbI}_4$  possess a direct bandgap of 2.59 eV, 2.18 eV and 1.84 eV using PBE functional. We find that the bandgaps of  $\text{Cs}_2\text{PbX}_4$  computed via PBE and HSE + SOC functionals are in good agreements with experiments and other theoretical results.<sup>9,10,27,28,35-38</sup> The band gap calculated by HSE is larger than PBE and the band gap calculated by PBE + SOC is smaller than PBE. In addition, the band gap of  $\text{MSe}_2$  calculated by HSE + SOC is larger than the related experimental data.<sup>27,28</sup> This is because the HSE functional usually overcorrects slightly the band gap of an intrinsic semiconductor.<sup>39</sup> Thus, in order to accurately and closely study the contact characteristics of  $\text{Cs}_2\text{PbX}_4\text{-MSe}_2$  heterostructures, PBE is employed in the following heterostructures section. When monolayers  $\text{Cs}_2\text{PbX}_4$  and  $\text{MSe}_2$  ( $\text{M} = \text{Mo}, \text{W}$ ) are contacted to make up  $\text{Cs}_2\text{PbX}_4\text{-MSe}_2$  heterostructures, the electronic structures of  $\text{Cs}_2\text{PbX}_4\text{-MSe}_2$  heterostructures are shown in Fig. 2. The  $\text{Cs}_2\text{PbCl}_4\text{-MoSe}_2$ ,  $\text{Cs}_2\text{PbBr}_4\text{-MoSe}_2$ ,  $\text{Cs}_2\text{PbI}_4\text{-MoSe}_2$ ,  $\text{Cs}_2\text{PbCl}_4\text{-WSe}_2$ ,  $\text{Cs}_2\text{PbBr}_4\text{-WSe}_2$  and  $\text{Cs}_2\text{PbI}_4\text{-WSe}_2$  heterostructures have an indirect bandgap with the value of 1.30 eV, 1.48 eV, 1.54 eV, 1.33 eV, 1.67 eV and 1.53 eV, which approach optimal bandgap (1.34 eV) for solar cells.<sup>40</sup> Moreover, the conduction band minimum (CBM) of  $\text{Cs}_2\text{PbX}_4\text{-MSe}_2$  heterostructures are dominated by the  $\text{MSe}_2$  layer and the valence band maximum (VBM) of  $\text{Cs}_2\text{PbX}_4\text{-MSe}_2$  heterostructures are dominated by  $\text{Cs}_2\text{PbX}_4$  part.

The analysis of energy level arrangement is of great significance to further study interface properties of  $\text{Cs}_2\text{PbX}_4\text{-MSe}_2$  heterostructures. The vacuum energy level ( $E_v$ ) is set to zero in the precontact state and the Fermi level ( $E_f$ ) is set to zero in the contact state. In precontact state, the CBM and VBM of monolayer  $\text{Cs}_2\text{PbX}_4$  are both higher than that of monolayer  $\text{MSe}_2$  and both  $\text{Cs}_2\text{PbX}_4\text{-MSe}_2$  are type-II heterostructures, as seen in Fig. 3(a). The electrons will diffuse from monolayers  $\text{Cs}_2\text{PbX}_4$  to monolayers  $\text{MSe}_2$  and the holes will move from monolayers  $\text{MSe}_2$  monolayer to monolayers  $\text{Cs}_2\text{PbX}_4$  when they contact. Correspondingly, the holes accumulate in  $\text{Cs}_2\text{PbX}_4$  monolayers and the electrons accumulate in  $\text{MSe}_2$  monolayers. Moreover, the difference between the vacuum level and the Fermi level is defined as the work function.<sup>31</sup> The work function is the internal dynamics of electron flow. The computed work functions of monolayers  $\text{Cs}_2\text{PbCl}_4$ ,  $\text{Cs}_2\text{PbBr}_4$ ,  $\text{Cs}_2\text{PbI}_4$ ,  $\text{MoSe}_2$  and  $\text{WSe}_2$  are 4.08 eV, 4.21 eV, 4.30 eV, 4.83 eV and 4.51 eV, respectively. The heterostructures are mainly related to the work function after contact. In order to maintain Fermi levels at the same level after contact, the Fermi level of all  $\text{Cs}_2\text{PbX}_4$  perovskites moved down and the Fermi level of monolayer  $\text{MSe}_2$  moved up after they contact each other.

The energy level diagram of  $\text{Cs}_2\text{PbX}_4\text{-MSe}_2$  heterostructures in contact states is given in Fig. 3(b). The  $\text{Cs}_2\text{PbX}_4\text{-MSe}_2$  heterostructures are type-II heterostructures, which can drive the photogenerated holes and electrons to move in opposite directions, resulting in spatial separation of holes and electrons on different sides of heterostructures.<sup>33</sup> Thus,  $\text{Cs}_2\text{PbX}_4\text{-MSe}_2$  heterostructures are beneficial for improving the photoelectric conversion efficiency of  $\text{Cs}_2\text{PbX}_4\text{-MSe}_2$  optoelectronic applications. In these type-II heterostructures, the differences between the VBM of their components (valence band offset,  $\Delta v$ ) are crucial for hole blocking and the differences between the CBM

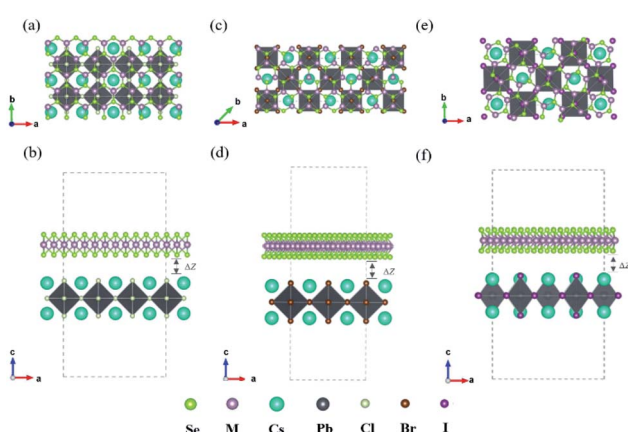


Fig. 1 Top and side views of relaxed  $\text{Cs}_2\text{PbX}_4\text{-MSe}_2$  ( $\text{M} = \text{Mo}, \text{W}$ ) heterostructures. (a and b)  $\text{Cs}_2\text{PbCl}_4\text{-MSe}_2$  heterostructure. (c and d)  $\text{Cs}_2\text{PbBr}_4\text{-MSe}_2$  heterostructure. (e and f)  $\text{Cs}_2\text{PbI}_4\text{-MSe}_2$  heterostructure.



**Table 1** Optimized lattice parameters ( $a$  and  $b$ ) and expanded cell lattice parameters ( $a_1$  and  $b_1$ ), lattice mismatch, interlayer distance  $\Delta Z$  and interface binding energy  $E_b$  of the relaxed  $\text{Cs}_2\text{PbX}_4$ – $\text{WSe}_2$  heterostructures

Heterostructures	$a$ (Å)	$b$ (Å)	$a_1$ (Å)	$b_1$ (Å)	Mismatch (%)	$\Delta Z$ (Å)	$E_b$ (meV Å $^{-2}$ )
$\text{Cs}_2\text{PbCl}_4$ – $\text{MoSe}_2$	16.51	5.66	16.75	5.69	1.10%	3.09	−16.73
$\text{Cs}_2\text{PbBr}_4$ – $\text{MoSe}_2$	16.35	11.81	16.65	11.89	0.62%	3.12	−16.28
$\text{Cs}_2\text{PbBr}_4$ – $\text{MoSe}_2$	18.22	8.66	18.14	8.84	1.79%	3.16	−16.12
$\text{Cs}_2\text{PbBr}_4$ – $\text{WSe}_2$	16.41	5.67	16.75	5.69	1.02%	2.90	−17.09
$\text{Cs}_2\text{PbBr}_4$ – $\text{WSe}_2$	16.35	11.81	16.65	11.89	0.65%	3.18	−17.52
$\text{Cs}_2\text{PbBr}_4$ – $\text{WSe}_2$	18.21	8.66	18.20	8.67	1.82%	3.30	−15.56

**Table 2** The bandgaps of monolayer  $\text{Cs}_2\text{PbX}_4$ ,  $\text{MoSe}_2$  and  $\text{WSe}_2$  by different calculation method

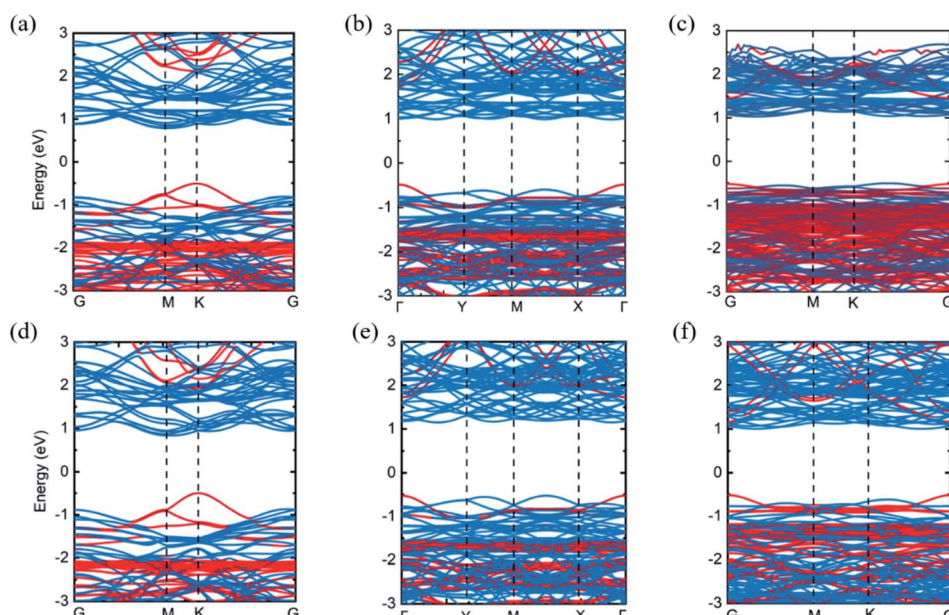
Functional	$\text{Cs}_2\text{PbCl}_4$	$\text{Cs}_2\text{PbBr}_4$	$\text{Cs}_2\text{PbI}_4$	$\text{MoSe}_2$	$\text{WSe}_2$
PBE	2.59	2.18	1.84	1.45	1.56
HSE	3.58	2.91	2.57	2.10	2.03
PBE + SOC	1.84	1.46	1.09	1.37	1.33
HSE + SOC	2.78	2.14	1.78	1.89	1.93
Experiment	3.01	2.32	1.86	1.48	1.60

of their components (conduction band offset,  $\Delta c$ ) are crucial for electron transport. The large  $\Delta v$  promotes hole extraction from TMDs layers to perovskite layers and the large  $\Delta c$  allows free electrons to move from perovskite to TMDs layers. It is shown that  $\text{Cs}_2\text{PbCl}_4$ – $\text{MSe}_2$  heterostructure have the largest  $\Delta c$  and  $\Delta v$  among  $\text{Cs}_2\text{PbX}_4$ – $\text{MSe}_2$  heterostructures.<sup>12</sup> Thus, the  $\text{Cs}_2\text{PbCl}_4$ – $\text{MoSe}_2$ , and  $\text{Cs}_2\text{PbCl}_4$ – $\text{WSe}_2$  heterostructures may have the largest charge transport power and are more conducive to reducing the dark current. In addition,  $\text{Cs}_2\text{PbX}_4$ – $\text{MoSe}_2$

heterostructures have larger  $\Delta c$  and  $\Delta v$  than  $\text{Cs}_2\text{PbX}_4$ – $\text{WSe}_2$  heterostructures.

In addition, the Mott–Wannier theory has been used to approximate exciton binding energies in the vdW heterostructures.<sup>41</sup> Table 3 lists the carrier masses and MW exciton binding energy of  $\text{Cs}_2\text{PbX}_4$ – $\text{MSe}_2$  heterostructures. The lower exciton binding energies usually facilitate the splitting of excitons into free charge carriers.<sup>34</sup> It is shown that  $\text{Cs}_2\text{PbCl}_4$ – $\text{MoSe}_2$  heterostructures exhibit the lowest exciton binding energies among  $\text{Cs}_2\text{PbX}_4$ – $\text{MoSe}_2$  heterostructures. Therefore,  $\text{Cs}_2\text{PbCl}_4$ – $\text{MoSe}_2$  heterostructures can effectively promote the separation of excitons and exhibit the highest charge transport efficiency among  $\text{Cs}_2\text{PbX}_4$ – $\text{MSe}_2$  heterostructures.

To clearly investigate the recombination rates of electron–hole pairs and transfer of charges between the  $\text{Cs}_2\text{PbX}_4$  monolayers and  $\text{MSe}_2$  monolayers across the interfaces, the plane-averaged charge density difference  $\Delta\rho$  are calculated, as shown in Fig. 4. The results demonstrate that the holes mainly accumulated at the  $\text{Cs}_2\text{PbX}_4$  interfaces and the charges accumulated at  $\text{MSe}_2$  interfaces. Additionally, the charges transfer

**Fig. 2** Band structures of  $\text{Cs}_2\text{PbX}_4$ – $\text{MSe}_2$  heterostructures (a)  $X = \text{Cl}$ ,  $M = \text{Mo}$ ; (b)  $X = \text{Br}$ ,  $M = \text{Mo}$ ; (c)  $X = \text{I}$ ,  $M = \text{Mo}$ ; (d)  $X = \text{Cl}$ ,  $M = \text{W}$ ; (e)  $X = \text{Br}$ ,  $M = \text{W}$ ; (f)  $X = \text{I}$ ,  $M = \text{W}$ . The red and blue lines correspond to  $\text{Cs}_2\text{PbX}_4$  and  $\text{MSe}_2$ , respectively.

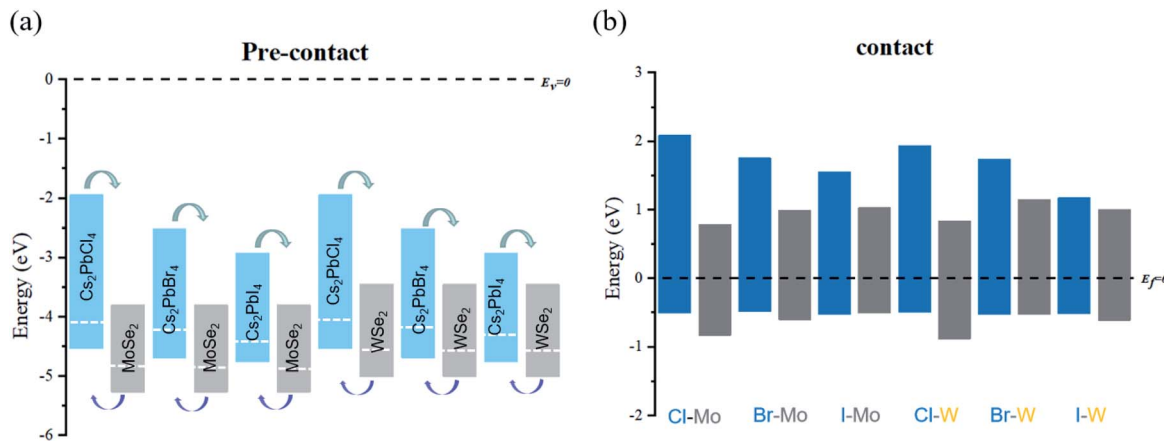


Fig. 3 Energy level graphs of the monolayer  $\text{MSe}_2$  and  $\text{Cs}_2\text{PbX}_4$  in the precontact (a) and contact (b). Blue and gray rectangles represent the monolayer  $\text{Cs}_2\text{PbX}_4$  and  $\text{MSe}_2$ . The bottom and top of rectangles correspond to VBM and CBM, respectively.

Table 3 Carrier effective masses ( $m_e$ ,  $m_h$ , and  $\mu_{\text{ex}}$ ), static dielectric constant ( $\epsilon$ ) and MW excitonic binding energies ( $E_{\text{eb}}$ )

Heterostructures	$m_e$ ( $m_0$ )	$m_h$ ( $m_0$ )	$\mu_{\text{ex}}$ ( $m_0$ )	$\epsilon$	$E_{\text{eb}}$ (eV)
$\text{Cs}_2\text{PbCl}_4\text{-MoSe}_2$	1.16	0.28	0.23	5.34	0.43
$\text{Cs}_2\text{PbBr}_4\text{-MoSe}_2$	0.79	0.71	0.37	5.44	0.68
$\text{Cs}_2\text{PbI}_4\text{-MoSe}_2$	1.39	0.67	0.45	5.24	1.00
$\text{Cs}_2\text{PbCl}_4\text{-WSe}_2$	1.46	0.27	0.23	4.95	0.50
$\text{Cs}_2\text{PbBr}_4\text{-WSe}_2$	0.75	0.66	0.35	5.08	0.74
$\text{Cs}_2\text{PbI}_4\text{-WSe}_2$	1.03	0.61	0.38	5.26	0.76

from  $\text{Cs}_2\text{PbX}_4$  interfaces to  $\text{MSe}_2$  interfaces while the holes move in the opposite direction. The direction of charge transfer

is consistent with that of band alignment analysis, which shown type-II heterostructures are benefited to the separation of electrons and holes. What's more, detail charge transfers among interlayer spacing are used to quantitatively evaluate charge transferring of heterostructures. The  $\text{Cs}_2\text{PbCl}_4\text{-MoSe}_2$ ,  $\text{Cs}_2\text{PbBr}_4\text{-MoSe}_2$ ,  $\text{Cs}_2\text{PbI}_4\text{-MoSe}_2$ ,  $\text{Cs}_2\text{PbCl}_4\text{-WSe}_2$ ,  $\text{Cs}_2\text{PbBr}_4\text{-WSe}_2$  and  $\text{Cs}_2\text{PbI}_4\text{-WSe}_2$  heterostructures have charge transfers among interlayer spacing with the values of 0.18, 0.15, 0.16, 0.16, 0.10 and  $0.14 \times 10^{-3}e$ . We find that the  $\text{Cs}_2\text{PbCl}_4\text{-MSe}_2$  heterostructures have the highest charge transfers in the six  $\text{Cs}_2\text{PbX}_4\text{-MSe}_2$  heterostructures among interlayer spacing. In addition,  $\text{Cs}_2\text{PbX}_4\text{-MoSe}_2$  heterostructures have larger charge transfers than  $\text{Cs}_2\text{PbX}_4\text{-WSe}_2$  heterostructures. It is because

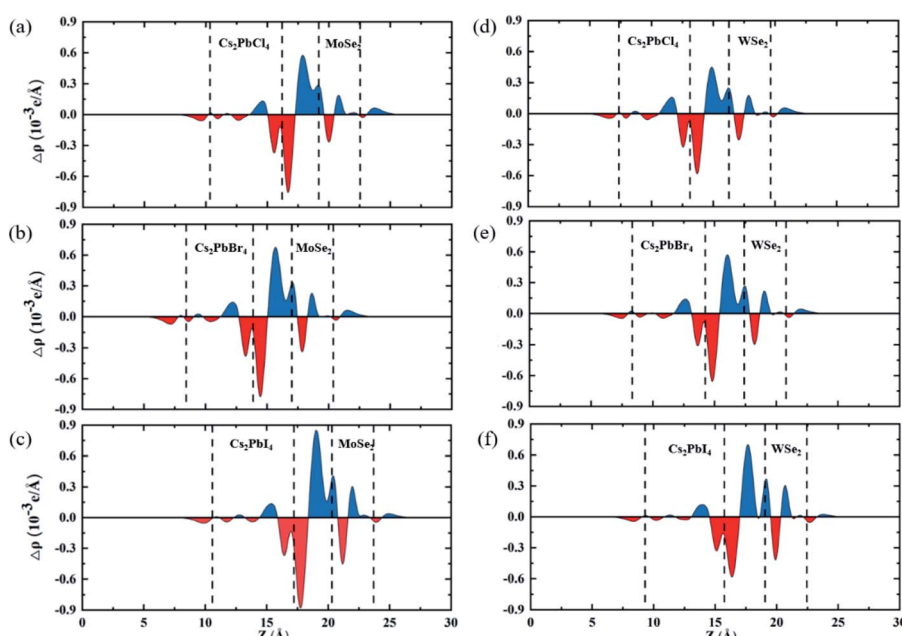


Fig. 4 The planar-averaged differential charge density  $\Delta\rho(z)$  of  $\text{Cs}_2\text{PbX}_4\text{-MSe}_2$  heterostructures: (a and d)  $X = \text{Cl}$ ; (b and e)  $X = \text{Br}$ ; (c and f)  $X = \text{I}$ . Red and blue represent electron depletion and accumulation.



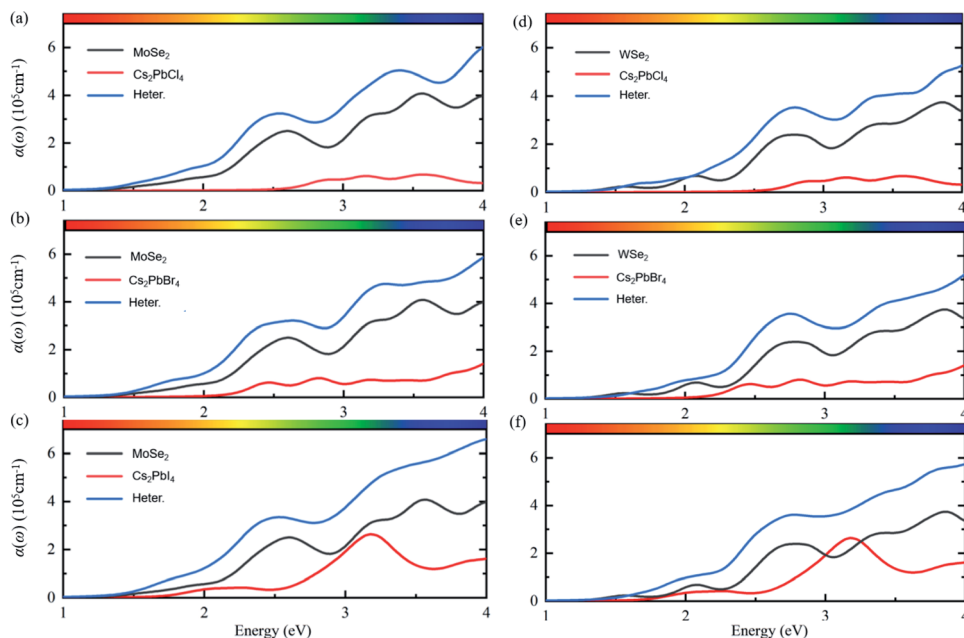


Fig. 5 Optical absorption coefficients of (a and d)  $\text{Cs}_2\text{PbCl}_4$ –MSe<sub>2</sub>, (b and e)  $\text{Cs}_2\text{PbBr}_4$ –MSe<sub>2</sub>, and (c and f)  $\text{Cs}_2\text{PbI}_4$ –MSe<sub>2</sub> heterostructures. The blue, black and red lines represent optical absorption spectrum of heterostructures, monolayer MSe<sub>2</sub> and Cs<sub>2</sub>PbX<sub>4</sub>, respectively.

Cs<sub>2</sub>PbX<sub>4</sub>–MoSe<sub>2</sub> heterostructures have smaller exciton binding energies than Cs<sub>2</sub>PbX<sub>4</sub>–WSe<sub>2</sub> heterostructures.

Except for the electronic structures and charge redistributions of heterostructures, the optical properties in vdW heterostructures have important effects on the performance of perovskite optoelectronic devices.<sup>42</sup> In order to further study the optical properties of Cs<sub>2</sub>PbX<sub>4</sub>–MSe<sub>2</sub> heterostructures, the optical absorption coefficients were calculated, as shown in Fig. 5. The optical absorption coefficients of MSe<sub>2</sub> monolayers are higher than those of Cs<sub>2</sub>PbX<sub>4</sub> monolayers. The optical absorption coefficients of all heterostructures are significantly higher than those of corresponding Cs<sub>2</sub>PbX<sub>4</sub> monolayers and

MSe<sub>2</sub> monolayers. This is because the bandgaps of 2D Cs<sub>2</sub>PbX<sub>4</sub>–MSe<sub>2</sub> heterostructures are smaller than the bandgaps of Cs<sub>2</sub>PbX<sub>4</sub> monolayers. The bandgaps of Cs<sub>2</sub>PbX<sub>4</sub>–MSe<sub>2</sub> heterostructures approach optimal bandgap (1.34 eV) for solar cells.<sup>40</sup> Thus, the construction of Cs<sub>2</sub>PbX<sub>4</sub>–MSe<sub>2</sub> heterostructures is beneficial to improve the light absorption of optoelectronic devices.

In addition, the light absorption of Cs<sub>2</sub>PbX<sub>4</sub>–MoSe<sub>2</sub> heterostructures is only slightly greater than that of Cs<sub>2</sub>PbX<sub>4</sub>–WSe<sub>2</sub> in the visible region because the light absorption of MoSe<sub>2</sub> is slightly greater than that of WSe<sub>2</sub> in the visible region. The light absorption coefficients of Cs<sub>2</sub>PbX<sub>4</sub> increase rapidly in the visible

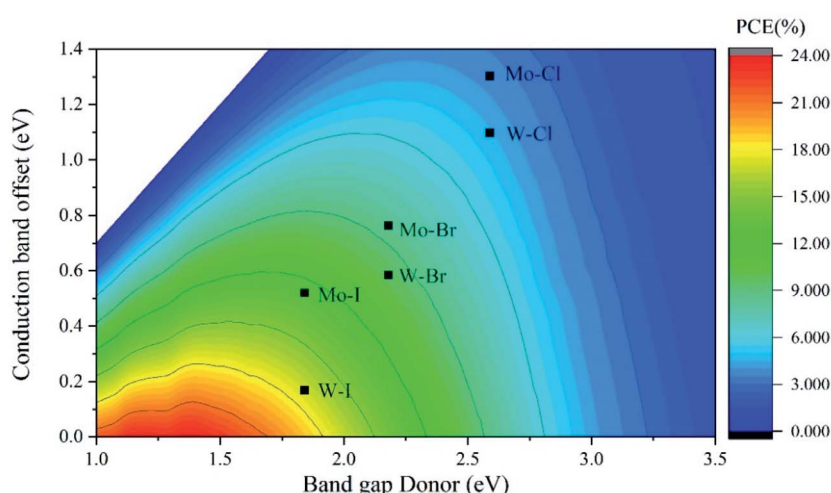


Fig. 6 Contour plot showing the calculated PCE of Cs<sub>2</sub>PbX<sub>4</sub>–MSe<sub>2</sub> heterostructures according to the Cs<sub>2</sub>PbX<sub>4</sub> donor band gap and conduction band offset  $\Delta c$ .



region with the halogen varying from Cl to I. The light absorption coefficients of  $\text{Cs}_2\text{PbX}_4\text{-MSe}_2$  heterostructures increase rapidly in the visible region with the halogen varying from Cl to I. Therefore, the  $\text{Cs}_2\text{PbI}_4\text{-MSe}_2$  heterostructure has great potential application in solar cells among  $\text{Cs}_2\text{PbX}_4\text{-MSe}_2$  heterostructures.

In order to explore the application of  $\text{Cs}_2\text{PbX}_4\text{-MSe}_2$  heterostructures in solar cells, we further calculated the power conversion efficiency of  $\text{Cs}_2\text{PbX}_4\text{-MSe}_2$  heterostructures. The PCE depends on the donor band gap and conduction band offset.<sup>43,44</sup> The PCE of  $\text{Cs}_2\text{PbX}_4\text{-MSe}_2$  heterostructures with type-II alignment is shown in Fig. 6 as a contour plot where the x- and y-axes are the donor band gap and conduction band offset, respectively. The PCE of  $\text{Cs}_2\text{PbI}_4\text{-MoSe}_2$ ,  $\text{Cs}_2\text{PbI}_4\text{-WSe}_2$  and  $\text{Cs}_2\text{PbBr}_4\text{-WSe}_2$  heterostructures is 13%, 18% and 10%, which is greater than 10%. Three heterostructures can be used in solar cells.  $\text{Cs}_2\text{PbI}_4\text{-WSe}_2$  heterostructure has the largest PCE (18%) among  $\text{Cs}_2\text{PbX}_4\text{-MSe}_2$  heterostructures. The PCE of  $\text{Cs}_2\text{PbI}_4\text{-WSe}_2$  heterostructure is larger than that of  $\text{WS}_2\text{/CsPbBr}_3$  PSCs (10.65%) and  $\text{WSe}_2$ -mediated PSCs (16.3%).<sup>13,18</sup> With the halogen varying from Cl to I, the PCE of  $\text{Cs}_2\text{PbX}_4\text{-WSe}_2$  heterostructures increase rapidly. The PCE variation trend is consistent with the absorption coefficients of  $\text{Cs}_2\text{PbX}_4\text{-MSe}_2$  heterostructures varying from Cl to I. In addition, the PCE of  $\text{Cs}_2\text{PbX}_4\text{-WSe}_2$  heterostructures is larger than the PCE of  $\text{Cs}_2\text{PbX}_4\text{-MoSe}_2$  heterostructures. This is mainly because  $\text{Cs}_2\text{PbX}_4\text{-WSe}_2$  heterostructures have smaller  $\Delta c$  than  $\text{Cs}_2\text{PbX}_4\text{-MoSe}_2$  heterostructures. Therefore,  $\text{Cs}_2\text{PbI}_4\text{-WSe}_2$  heterostructure has great potential application in solar cells.

## Conclusions

In summary, we have systematically studied the structural, stability, charge transfer and optoelectronic properties of 2D perovskite  $\text{Cs}_2\text{PbX}_4\text{-MSe}_2$  heterostructures with different halide elements based on density functional calculations. All these six heterostructures are stable in energy and the interlayer distances increase gradually with the halogen varying from Cl to I. Electronic structures show  $\text{Cs}_2\text{PbX}_4\text{-MSe}_2$  heterostructures belongs to type-II energy level shifts with narrower optical gap than monolayers  $\text{Cs}_2\text{PbX}_4$ . In addition, the  $\text{Cs}_2\text{PbCl}_4\text{-MoSe}_2$ , and  $\text{Cs}_2\text{PbCl}_4\text{-WSe}_2$  heterostructures may have the largest charge transport power due to their larger band offset, which is beneficial to reduce dark current and improve open circuit voltage.  $\text{Cs}_2\text{PbCl}_4\text{-MoSe}_2$  heterostructures can effectively promotes the separation of excitons and exhibit the highest charge transport efficiency among  $\text{Cs}_2\text{PbX}_4\text{-MSe}_2$  heterostructures due to their lowest exciton binding energies.  $\text{Cs}_2\text{PbCl}_4\text{-MoSe}_2$  heterostructure has the potential to be applied in photodetectors. Next, the charges transfer from  $\text{Cs}_2\text{PbX}_4$  interfaces to  $\text{MSe}_2$  interfaces while the holes move in the opposite direction. The holes mainly accumulated at the  $\text{Cs}_2\text{PbX}_4$  interfaces and the charges accumulated at  $\text{MSe}_2$  interfaces.  $\text{Cs}_2\text{PbX}_4\text{-MoSe}_2$  heterostructures have larger charge transfers than  $\text{Cs}_2\text{PbX}_4\text{-WSe}_2$  heterostructures. Finally, optical absorptions of six heterostructures are significantly higher than the corresponding  $\text{Cs}_2\text{PbX}_4$  monolayers and  $\text{MSe}_2$  monolayers. The PCE

of  $\text{Cs}_2\text{PbX}_4\text{-WSe}_2$  heterostructures is larger than the PCE of  $\text{Cs}_2\text{PbX}_4\text{-MoSe}_2$  heterostructures.  $\text{Cs}_2\text{PbI}_4\text{-WSe}_2$  heterostructure has the largest PCE (18%) among  $\text{Cs}_2\text{PbX}_4\text{-MSe}_2$  heterostructures. In conclusion,  $\text{Cs}_2\text{PbCl}_4\text{-MoSe}_2$  heterostructure exhibits great potential application in photodetectors devices and  $\text{Cs}_2\text{PbI}_4\text{-WSe}_2$  heterostructure has great potential application in solar cells. Our findings provide insight into of  $\text{Cs}_2\text{PbX}_4\text{-MSe}_2$  heterostructures can effectively improve the performance of perovskite optoelectronic devices.

## Conflicts of interest

There are no conflicts to declare.

## Acknowledgements

This work is supported by the Fund of State Key Laboratory of IPOC(BUPT) (no. IPOC2019ZZ04) and the Open-Foundation of Key Laboratory of Laser Device Technology, China North Industries Group Corporation Limited (Grant No. KLLDT202103). We thank for the helpful discussion with Prof. Pengfei Guan and the computational support from the Beijing Computational Science Research Center (CSRC). We also acknowledge the computation supported by High-performance Computing Platform of BUPT.

## Notes and references

- 1 A. T. Barrows, A. J. Pearson, C. K. Kwak, A. D. F. Dunbar, A. R. Buckley and D. G. Lidzey, *Energy Environ. Sci.*, 2014, **7**, 2944–2950.
- 2 K. Xiao, R. Lin, Q. Han, Y. Hou, Z. Qin, H. T. Nguyen, J. Wen, M. Wei, V. Yeddu, M. I. Saidaminov, Y. Gao, X. Luo, Y. Wang, H. Gao, C. Zhang, J. Xu, J. Zhu, E. H. Sargent and H. Tan, *Nat. Energy*, 2020, **5**, 870–880.
- 3 I. L. Braly, D. W. deQilettes, L. M. Pazos-Outon, S. Burke, M. E. Ziffer, D. S. Ginger and H. W. Hillhouse, *Nat. Photonics*, 2018, **12**, 355–361.
- 4 M. M. Lee, J. Teuscher, T. Miyasaka, T. N. Murakami and H. J. Snaith, *Science*, 2012, **338**, 643–647.
- 5 J. H. Noh, S. H. Im, J. H. Heo, T. N. Mandal and S. I. Seok, *Nano Lett.*, 2013, **13**, 1764–1769.
- 6 Y.-Y. Zhang, S. Chen, P. Xu, H. Xiang, X.-G. Gong, A. Walsh and S.-H. Wei, *Chin. Phys. Lett.*, 2018, **35**, 036104.
- 7 S. Chen and G. Shi, *Adv. Mater.*, 2017, **29**, 1605448.
- 8 Y. F. Ding, Q. Q. Zhao, Z. L. Yu, Y. Q. Zhao, B. Liu, P. B. He, H. Zhou, K. L. Li, S. F. Yin and M. Q. Cai, *J. Mater. Chem. C*, 2019, **7**, 7433–7441.
- 9 A. Bala, A. K. Deb and V. Kumar, *J. Phys. Chem. C*, 2018, **122**, 7464–7473.
- 10 J. Song, L. Xu, J. Li, J. Xue, Y. Dong, X. Li and H. Zeng, *Adv. Mater.*, 2016, **28**, 4861–4869.
- 11 E. Shi, Y. Gao, B. P. Finkenauer, A. Akriti, A. H. Coffey and L. Dou, *Chem. Soc. Rev.*, 2018, **47**, 6046–6072.
- 12 J. He, J. Su, Z. Lin, S. Zhang, Y. Qin, J. Zhang, J. Chang and Y. Hao, *J. Phys. Chem. C*, 2019, **123**, 7158–7165.



13 Q. W. Zhou, J. L. Duan, X. Y. Yang, Y. Y. Duan and Q. W. Tang, *Angew. Chem., Int. Ed.*, 2020, **132**, 22181–22185.

14 J. P. Cao, G. Q. Tang, P. You, T. Y. Wang, F. Y. Zheng, J. Zhao and F. Yan, *Adv. Funct. Mater.*, 2020, **30**, 2002358.

15 Hybrid Bilayer WSe<sub>2</sub>–CH<sub>3</sub>NH<sub>3</sub>PbI<sub>3</sub> Organolead Halide Perovskite as a High-Performance Photodetector.

16 S. Hassan, P. Basera, S. Bera, M. Mittal, S. K. Ray, S. Bhattacharya and S. Sapra, *ACS Appl. Mater. Interfaces*, 2020, **12**, 7217–7325.

17 S.-H. Lee, J. Y. Kim, S. Choi, Y. Lee, K.-S. Lee, J. Kim and J. Joo, *ACS Appl. Mater. Interfaces*, 2020, **12**, 25159–25167.

18 Y. Choi, S. Jung, N. K. Oh, J. Lee, J. Seo, U. Kim, D. Koo and H. Park, Enhanced charge transport via metallic 1T phase transition metal dichalcogenides-mediated hole transport layer engineering for perovskite solar cells, *Chemnanomat*, 2019, **5**, 1050–1058.

19 G. Kresse and D. Joubert, *Phys. Rev. B: Condens. Matter Mater. Phys.*, 1999, **59**, 1758–1775.

20 J. P. Perdew, K. Burke and M. Ernzerhof, *Phys. Rev. Lett.*, 1996, **77**, 3865–3868.

21 P. E. Blochl, *Phys. Rev. B: Condens. Matter Mater. Phys.*, 1994, **50**, 17953–17979.

22 B. Jia, P. Zhu, S. Sun, L. Han, G. Liu, Y. Wang, G.-D. Peng and P. Lu, *IEEE J. Sel. Top. Quantum Electron.*, 2019, **26**, 1–6.

23 S. Lin, J. C. Liu, W. Z. Li, D. Wang, Y. Huang, C. Jia, Z. W. Li, H. Y. Wang, J. N. Song, Z. L. Liu, K. Huang, D. Zu, M. Lei, B. Hong and H. Wu, *Nano Lett.*, 2019, **19**, 6853–6861.

24 J. C. Xu, K. Bi, R. Zhang, Y. N. Hao, C. W. Lan, M.-M. Klaus, X. J. Zhai, Z. D. Zhang and S. G. H, *Research*, 2019, **2019**, 9686213.

25 X. N. Guan, R. Zhang, B. N. Jia, L. Y. Wu, B. Zhou, L. Fan, G. Liu, Y. Wang, P. F. Lu and G. D. Peng, *J. Non-Cryst. Solids*, 2020, **550**, 120388.

26 P. F. Lu, *J. Sichuan Norm. Univ., Nat. Sci.*, 2020, **43**, 1–20.

27 X. Wang, Y. Gong, G. Shi, W. L. Chow, K. Keyshar, G. Ye, R. Vajtai, J. Lou, Z. Liu, E. Ringe, B. K. Tay and P. M. Ajayan, *ACS Nano*, 2014, **8**, 5125–5131.

28 J.-K. Huang, J. Pu, C.-L. Hsu, M.-H. Chiu, Z.-Y. Juang, Y.-H. Chang, W.-H. Chang, Y. Iwasa, T. Takenobu and L.-J. Li, *ACS Nano*, 2014, **8**(1), 923–930.

29 J.-H. Yang, Q. Yuan and B. I. Yakobson, *J. Phys. Chem. C*, 2016, **120**, 24682–24687.

30 Y.-Q. Zhao, Y. Xu, D.-F. Zou, J.-N. Wang, G.-F. Xie, B. Liu, M.-Q. Cai and S.-L. Jiang, *J. Phys.: Condens. Matter*, 2020, **32**, 195501.

31 Y. Ding, Y. Wang, J. Ni, L. Shi, S. Shi and W. Tang, *Phys. Chem. Chem. Phys.*, 2011, **13**, 15546–15553.

32 Y. Zhang, Y. Zhao, Y. Xu and L. He, *Solid State Commun.*, 2021, **327**, 114233.

33 B. Liu, M. Long, M.-Q. Cai and J. Yang, *J. Phys. Chem. Lett.*, 2018, **327**, 114233.

34 J. H. Chen, X. J. He, B. S. Sa, J. Zhou, C. Xu, C. L. Wen and Z. M. Sun, *Nanoscale*, 2019, **11**, 6431–6444.

35 P. Zhu, H. Zhao, X. Li, Y. Zu, L. Wu, C. Chen and G. Liu, *Phys. E*, 2021, **134**, 114908.

36 A. Molina-Sánchez, *ACS Appl. Energy Mater.*, 2018, **1**, 6361–6367.

37 Z. Zheng, X. X. Wang, Y. W. Shen, Z. Y. Luo, L. G. Li, L. Gan, Y. Ma, H. Q. Li, A. L. Pan and T. Y. Zhai, *Adv. Opt. Mater.*, 2018, **6**, 1800879.

38 P. B. Gui, H. Zhou, F. Yao, Z. H. Song, B. R. Li and G. J. Fang, *Small*, 2019, **15**, 1902618.

39 R. J. Sutton, M. R. Filip, A. A. Haghaghirad, N. Sakai, B. Wenger, F. Giustino and H. J. Snaith, *ACS Energy Lett.*, 2018, **3**, 1787–1794.

40 S. Ruhle, *Sol. Energy*, 2016, **130**, 139–147.

41 P. Wang, Y. X. Zong, H. Liu, H. Y. Wen, H. X. Deng, Z. M. Wei, H. B. Wu and J. B. Xia, *J. Phys. Chem. C*, 2020, **214**, 23832–23838.

42 W. J. Yin, J. H. Yang, J. Kang, Y. Yan and S. H. Wei, *J. Mater. Chem. A*, 2015, **3**, 8926–8942.

43 M. C. Scharber, D. Wuhlbacher, M. Koppe, P. Denk, C. Waldauf, A. J. Heeger and C. L. Brabec, *Adv. Mater.*, 2006, **18**, 189.

44 M. Bernardi, M. Palummo and J. C. Grossman, *ACS Nano*, 2012, **6**, 10082–10089.

